Scilight

eChem

https://www.sciltp.com/journals/eChem

Article

Atomically Precise Ag_9Cu_6 and Ag_{15} Nanoclusters for Nitrate Electroreduction to NH_3: Probing the Cu Doping Effect

Jiaming Tan [1,†], Yingwei Li [2,*,†], Liang Qiao [3,†], Jingwen Yang [1], Tao Wu [1], Lubing Qin [1], Ruihao Huang [1], Chunsheng Yang [3], Kebin Chi [3,*] and Zhenghua Tang [1,*]

[1] New Energy Research Institute, School of Environment and Energy, South China University of Technology, Guangzhou Higher Education Mega Centre, Guangzhou 510006, China
[2] Department of Chemistry, University of Hawai'i at Manoa, Bilger 321A, 2545 McCarthy Mall, Honolulu, HI 96822, USA
[3] Petrochemical Research Institute, PetroChina Company Limited, Beijing 102206, China
* Correspondence: yingweil@hawaii.edu (Y.L.); ckb459@petrochina.com.cn (K.C.); zhht@scut.edu.cn (Z.T.)
† These authors contributed equally to this work.

How To Cite: Tan, J.; Li, Y.; Qiao, L.; et al. Atomically Precise Ag_9Cu_6 and Ag_{15} Nanoclusters for Nitrate Electroreduction to NH_3: Probing the Cu Doping Effect. *eChem* **2026**, *2*(1), 6. https://doi.org/10.53941/echem.2026.100006

Received: 22 April 2026
Revised: 24 May 2026
Accepted: 11 June 2026
Published: 24 June 2026

Abstract: Ammonia (NH_3) is an essential chemical feedstock and promising energy carrier. However, the traditional Haber-Bosch process remains highly energy intensive and carbon emitting, motivating the development of sustainable alternatives. Electrochemical nitrate reduction (eNO_3RR) has emerged as an attractive route for green NH_3 synthesis because nitrate is highly soluble and easier to activate than N_2. Yet achieving high NH_3 selectivity remains challenging due to the complex eight-electron, nine-proton transfer pathway. Although bimetallic catalysts can improve the catalytic performance, conventional heterogeneous systems often suffer from their non-uniform surface structures and ill-defined active sites, hindering the elucidation of structure-property relationships. Herein, we reveal the mechanism of heterometal doping on eNO_3RR at the atomic level using atomically precise alkynyl-protected homometallic Ag_{15} and bimetallic Ag_9Cu_6 nanoclusters. Cu atoms selectively occupy the six outer octahedral vertex sites, forming a well-defined $Ag_1@Ag_8@Cu_6$ framework and creating an accessible bimetallic surface microenvironment for electrocatalysis. Ag_9Cu_6 delivers markedly enhanced eNO_3RR performance, achieving an NH_3 Faradaic efficiency of 88.48% and a yield rate of 9.93 $mg \cdot h^{-1} \cdot cm^{-2}$ at –0.6 V vs. RHE, about 2.6 times higher than Ag_{15}, together with excellent stability. *In situ* attenuated total reflection surface-enhanced infrared absorption spectroscopy (ATR-SEIRAS) clearly reveals hydrogenation of $^*NH_2$ is the rate-determining step as Ag_{15} suffers from accumulation of sluggish $^*NH_2$. In contrast, the Ag–Cu active sites in Ag_9Cu_6 promote deep hydrogenation and $^*NH_3$ desorption while suppressing the hydrogen evolution reaction. This work provides mechanistic insight into a design paradigm for atomically precise Ag–Cu bimetallic electrocatalysts toward selective NH_3 synthesis.

Keywords: electrochemical nitrate reduction; ammonia synthesis; Ag–Cu nanoclusters; heterometal doping effect; structure-property relationship

1. Introduction

Ammonia (NH_3) is an essential feedstock for modern agriculture and the chemical industry, and it is also attracting increasing interest as a carbon-free energy carrier [1,2]. Industrial NH_3 production, however, still relies overwhelmingly on the Haber-Bosch (H-B) process [3,4], which operates under harsh conditions and remains highly energy intensive and carbon emitting [5]. The conventional process is responsible for a measurable fraction of global anthropogenic CO_2 emissions, underscoring the need for more sustainable synthetic routes. Electrochemical NH_3 synthesis has therefore emerged as a highly attractive alternative because it can, in principle, be powered by renewable electricity under ambient conditions [2,6,7]. Current efforts mainly focus on two pathways—the electrochemical nitrogen reduction reaction (eNRR) and the electrochemical nitrate reduction reaction (eNO_3RR) [5,8]. Among them, eNO_3RR is generally considered as the more practical route since the strong N≡N triple bond possesses an exceptionally high bond dissociation energy (941 $kJ\cdot mol^{-1}$), and low solubility of N_2 severely limit the efficiency of eNRR [4,9], whereas nitrate ion (NO_3^-) offers much higher aqueous solubility and lower bond dissociation energies (245 $kJ\cdot mol^{-1}$), making eNO_3RR thermodynamically more favorable with substantially higher NH_3 production rates [3,9,10]. As a result, eNO_3RR has rapidly emerged as a promising strategy for sustainable NH_3 production, although achieving high NH_3 selectivity across its complex multi-electron transfer pathway remains a major challenge [3,11,12].

Mechanistically, eNO_3RR is an eight-electron, nine-proton reduction process that proceeds through multiple intermediates and competing pathways, producing byproducts such as NO_2^-, N_2, N_2H_4, and H_2 [13–16]. A clear understanding of the reaction mechanism is therefore critical for identifying the rate-determining steps, improving selectivity, and guiding catalyst design [6,17–21]. Noble-metal catalysts such as Pt, Pd, and Au have shown excellent activity and selectivity in eNO_3RR because of their favorable electronic structures and intermediate binding affinities [22–25]. However, their scarcity and high cost limit practical deployment [26–29]. This has motivated growing interest in earth-abundant alternatives, especially Cu- and Ag-based systems [28,30–33]. In particular, alloying has proven to be an effective strategy for enhancing the catalytic performance through synergistic effects [29,34]. However, conventional bimetallic nanoparticles are not uniform at atomic level, and their ill-defined surface structures and uncertain atomic distributions make it difficult to identify the true active-sites or establish the rigorous structure-property relationship when applied as electrocatalysts [21,35,36].

Atomically precise metal nanoclusters (NCs) provide a powerful platform to address this challenge [21,37–40]. Unlike conventional nanoparticles, metal NCs feature exact atomic compositions, well-defined geometries, and tailorable surface environments [36,39,41], enabling mechanistic studies at the molecular and atomic levels [39,40,42]. Recent work has shown that even subtle structural perturbations, such as the addition of a single metal atom (Cu_{13} vs. Cu_{14}) [38]. or targeted heteroatom substitution [21,41,43], can lead to pronounced changes in catalytic performance. Such precision makes metal NCs particularly attractive for uncovering how heteroatom doping regulates the d-band center and local electron density, and thereby the catalytic selectivity via tuning the adsorption thermodynamics of key intermediates. Nevertheless, the application of atomically precise bimetallic NCs to eNO_3RR, especially Cu-Ag systems, remains largely unexplored, and the role of heteroatom doping in controlling NH_3 selectivity is yet not well understood.

Herein, we address the issue using two 3,3-dimethyl-1-butyne (^{t}Bu-C≡C) protected NCs, the monometallic $Ag_{15}(C{\equiv}C^tBu)_{12}^+$ and the bimetallic $Ag_9Cu_6(C{\equiv}C^tBu)_{12}^+$ of the same structure but different atomic composition [44,45]. The incorporation of six Cu atoms into the Ag framework generates a robust $Ag_1@Ag_8@Cu_6$ architecture with distinct electronic property and surface environment [44,45]. Electrochemical evaluations highlight that Cu doping leads to a pronounced enhancement in eNO_3RR performance. While Ag_{15} reaches a maximum NH_3 Faradaic efficiency (FE) of 69.24% with a yield rate of 3.76 mg h^{-1} cm^{-2} at –0.5 V vs. RHE, Ag_9Cu_6 delivers a significantly improved FE_{NH_3} of 88.48% at –0.6 V vs. RHE and a yield rate of 9.93 $mg\cdot h^{-1}\cdot cm^{-2}$. Notably, these optimal values occur at different applied potentials, reflecting the distinct electrocatalytic characteristics of the two NCs. Combined with *in situ* ATR-SEIRAS analysis, our results reveal how the synergistic Ag-Cu sites promote nitrate activation by reducing the energy barriers while suppressing the competing hydrogen evolution reaction (HER). This work establishes a clear structure-activity relationship at atomic-level for bimetallic NCs in eNO_3RR and provides mechanistic guidance for the rational design of selective electrocatalysts for sustainable NH_3 synthesis.

2. Results and Discussion

2.1. Preparation and Characterization of Ag_{15} and Ag_9Cu_6 Nanoclusters

$Ag_{15}(C{\equiv}C^tBu)_{12}^+$ was synthesized via a synchronous nucleation-passivation strategy [44]. In a typical procedure, solution A containing 136 mg CF_3CO_2Ag in 15 mL dichloromethane and 1 mL acetonitrile, solution B containing 83 mg CH_3ONa and ^{t}BuC≡CH (15 μL) in 2 mL methanol, solution C containing 144 mg $NaBH_3CN$ in 10 mL MeOH were prepared separately. Under vigorous stirring, solution B was added into solution A to yield a colorless suspension, followed by the rapid injection of solution C. An immediate color transition to purple was observed, indicating the formation of NCs. The reaction was kept in an ice bath for 3 h. Then, the solvent was removed via rotary evaporation, and the crude solid was extracted and purified using a DCM/acetonitrile mixture to give Ag_{15} as a purple solution.

$\mathrm{^{t}BuC{\equiv}CAg(I)}$ precursor was synthesized via a previously reported method [45]. Briefly, $\mathrm{Ag_2O}$ (500 mg, 2.1 mmol) was suspended in 20 mL of aqueous ammonia and kept vigorously stirring for 10 min until complete dissolution. After filtration, 5 mL of deionized water was added into the filtrate and $\mathrm{^{t}Bu\text{-}C{\equiv}CH}$ (950 mg, 4.1 mmol in 2.5 mL of ethanol) was added dropwise under vigorous stirring (1000 rpm) over 10 min. The white precipitate was washed repeatedly with deionized water, ethanol, and diethyl ether, and collected via centrifugation to yield $\mathrm{^{t}BuC{\equiv}CAg(I)}$. In a typical synthesis of $\mathrm{Ag_9Cu_6(C{\equiv}C^{t}Bu)_{12}^{+}}$, $\mathrm{^{t}BuC{\equiv}CAg(I)}$ (6.30 mg, 0.03 mmol) and $\mathrm{NaSbF_6}$ (7.84 mg, 0.03 mmol) were ultrasonically co-dispersed in 4 mL DCM and 2 mL MeCN at room temperature. After 10 min, a freshly prepared solution of $\mathrm{(PPh_3)_2CuBH_4}$ was added under vigorous stirring for an additional 10 min. The solution color changed from colorless to yellow and eventually to dark brown. The mixture was incubated for 12 h in the absence of light. The solvent was removed via rotary evaporation and the dark solid was washed with ethyl acetate and methanol extensively. $\mathrm{Ag_9Cu_6(C{\equiv}C^{t}Bu)_{12}^{+}}$ were then extracted with DCM to give a blue solution.

The synthesis of monometallic $\mathrm{Ag_{15}(C{\equiv}C^{t}Bu)_{12}^{+}}$ ($\mathrm{Ag_{15}}$) and bimetallic $\mathrm{Ag_9Cu_6(C{\equiv}C^{t}Bu)_{12}^{+}}$ ($\mathrm{Ag_9Cu_6}$) NCs is verified by UV-vis absorbance spectroscopy (Figure 1a,b) and electrospray ionization mass spectrometry (ESI-MS, Figure 1c,d), confirming the high purity of the product and atomic composition consistent with the literatures [44,45]. Single-crystal X-ray diffraction (SC-XRD) reveals the key structural distinction between $\mathrm{Ag_{15}}$ and $\mathrm{Ag_9Cu_6}$ is the substitution of 6 outer octahedral Ag sites by Cu atoms, giving rise to an $\mathrm{Ag_1@Ag_8@Cu_6}$ configuration (Figure 1e) [44,45]. Therefore, the triple absorption peaks are observed in the spectra of both NCs although Cu doping results in a general red-shift of the three peaks in $\mathrm{Ag_9Cu_6}$ (Figure 1a,b).

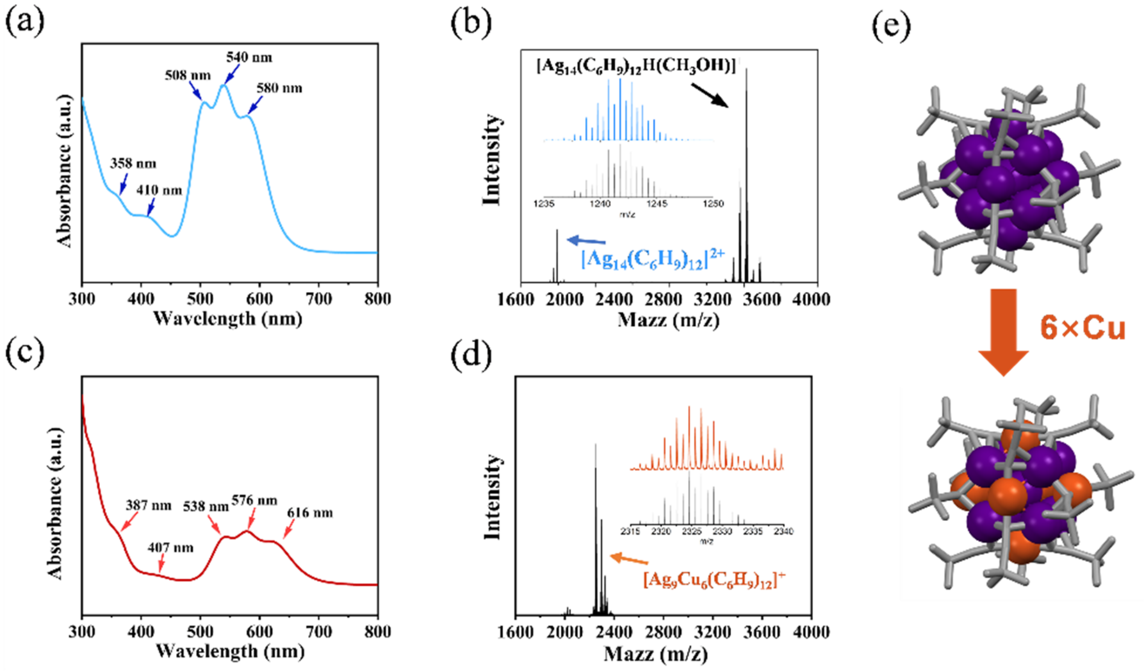

Figure 1. (**a**) UV-vis absorption spectrum and (**b**) ESI-MS spectrum of $\mathrm{Ag_{15}(C{\equiv}C^{t}Bu)_{12}^{+}}$. (**c**) UV-vis absorption spectrum and (**d**) ESI-MS spectrum of $\mathrm{Ag_9Cu_6(C{\equiv}C^{t}Bu)_{12}^{+}}$. (**e**) Crystal structures of $\mathrm{Ag_{15}(C{\equiv}C^{t}Bu)_{12}^{+}}$ (top) and $\mathrm{Ag_9Cu_6(C{\equiv}C^{t}Bu)_{12}^{+}}$ (bottom) NCs. Color code: purple = Ag; brown = Cu; grey = C, H is omitted for clarity.

In $\mathrm{Ag_{15}(C{\equiv}C^{t}Bu)_{12}^{+}}$, the highly symmetric and robust metal core is stabilized by 12 alkynyl ligands. The core consists of a body-centered cubic (BCC) $\mathrm{Ag_1@Ag_8}$ unit, which is further capped by six Ag on the square facets, affording a highly symmetric NC scaffold in the trigonal *R-3* space group. This well-defined framework provides an ideal template for site-selective heterometal doping. Relative to the parent $\mathrm{Ag_{15}(C{\equiv}C^{t}Bu)_{12}^{+}}$, $\mathrm{Ag_9Cu_6(C{\equiv}C^{t}Bu)_{12}^{+}}$ preserves both the 15-metal-atom framework and the 12 ligands, differing only in its highly regioselective doping pattern. Specifically, the Cu atoms exclusively occupy the outer six octahedral vertex sites, surrounding the inner BCC $\mathrm{Ag_1@Ag_8}$ core. This substitution is favored by the smaller atomic radius of Cu relative to Ag. As a result, Cu incorporation induces a slight contraction at the peripheral sites and thereby modulates the electronic structure of the NC. Cu doping preserves the structural integrity of the rigid BCC core while generating highly exposed adjacent Cu–Ag sites on the cluster surface, providing bimetallic microenvironment that plays a critical role in regulating the reactant adsorption and promoting the subsequent catalytic processes.

2.2. Electrochemical Performance

Details on electrode fabrication and assembly are given in Supplementary Materials. To assess the electrocatalytic activity and selectivity of Ag_{15} and Ag_9Cu_6 catalysts, linear sweep voltammetry (LSV) and potentiostatic electrolysis were carried out in 1.0 M KOH containing 0.1 M KNO_3 (pH = 14). Unless otherwise noted, all potentials are reported versus the reversible hydrogen electrode (RHE). An alkaline electrolyte was deliberately chosen because it favours eNO_3RR while suppressing competing proton-coupled side reactions, most notably the HER [13,16,17]. The calibration curves for NH_3 and NO_2^- quantification in the alkaline nitrate electrolyte matrix are given in Figures S1 and S2.

Taking $Ag_{15}(C{\equiv}C^tBu)_{12}^+$ as the monometallic reference, we examined the electrocatalytic behavior of the bimetallic $Ag_9Cu_6(C{\equiv}C^tBu)_{12}^+$. Linear sweep voltammetry (LSV) was employed to probe the catalytic response toward nitrate reduction. In the nitrate-free electrolyte, Ag_9Cu_6 exhibits a higher cathodic background current density compared to Ag_{15} (Figure 2a). This enhanced geometric response is collaborated with double-layer capacitance C_{dl} measurements, where Ag_9Cu_6 yields a markedly larger C_{dl} value than Ag_{15} (Figure 2b,c vs. Figure 2e,f), indicating an expanded electrochemically active surface area (ECSA). Upon addition of 0.1 M KNO_3, the polarization curves for both catalysts exhibit a pronounced anodic shift together with a substantial increase in cathodic current density (Figure 2d), confirming the initiation of the electrochemical nitrate reduction reaction. Notably, Ag_9Cu_6 displays a significantly larger current density enhancement across the applied potential range when NO_3^- is present, reaching 335 $mA{\cdot}cm^{-2}$ at –1.0 V vs. RHE, compared with 178 $mA{\cdot}cm^{-2}$ in nitrate-free electrolyte (Figure 2a). In contrast, Ag_{15} delivers 175 $mA{\cdot}cm^{-2}$ under the same conditions, only slightly higher than its background response (160 $mA{\cdot}cm^{-2}$). Collectively, these results demonstrate that, relative to Ag_{15}, Ag_9Cu_6 facilitates highly efficient nitrate activation and substantially lowers the kinetic barrier for eNO_3RR, and thereby exhibiting superior electrocatalytic performance.

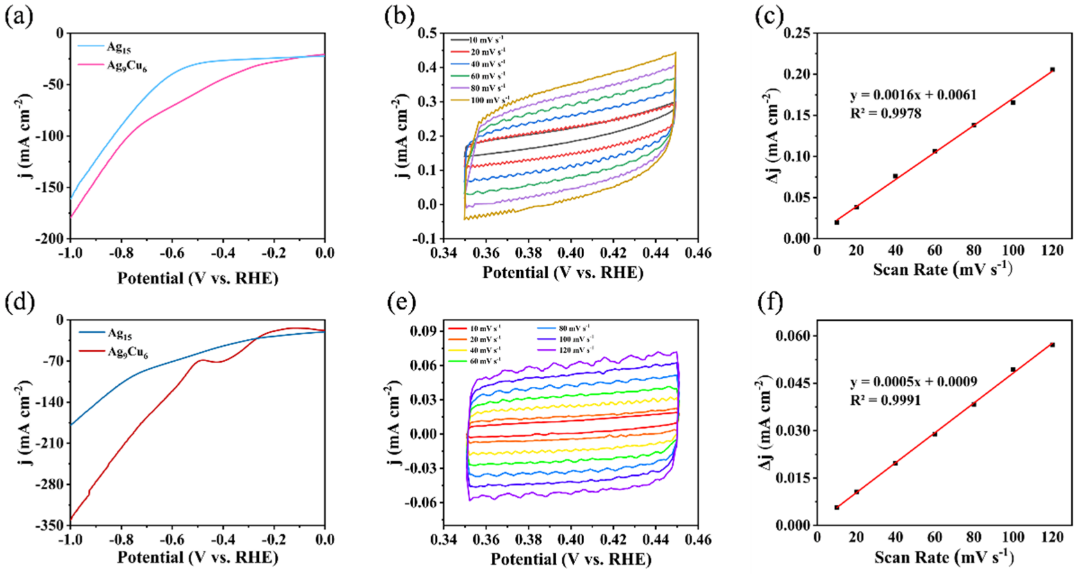

Figure 2. (**a**) LSV curves of $Ag_{15}(C{\equiv}C^tBu)_{12}^+$ and $Ag_9Cu_6(C{\equiv}C^tBu)_{12}^+$ in 1.0 M KOH electrolyte without KNO_3. (**b**) CV curves of $Ag_9Cu_6(C{\equiv}C^tBu)_{12}^+$ measured at various scan rates in the non-Faradaic region and (**c**) corresponding C_{dl} linear fit. (**d**) LSV curves of $Ag_{15}(C{\equiv}C^tBu)_{12}^+$ and $Ag_9Cu_6(C{\equiv}C^tBu)_{12}^+$ in 1.0 M KOH electrolyte with 0.1 M KNO_3. (**e**) CV curves of $Ag_{15}(C{\equiv}C^tBu)_{12}^+$ measured at various scan rates in the non-Faradaic region and (**f**) corresponding C_{dl} linear fit.

The product selectivity of $Ag_{15}(C{\equiv}C^tBu)_{12}^+$ and $Ag_9Cu_6(C{\equiv}C^tBu)_{12}^+$ was then evaluated over a range of applied potentials (Figure 3). For both catalysts, the Faradaic efficiencies (FE) for ammonia (FE_{NH_3}) exhibited a characteristic volcano-type dependence on potential. For Ag_{15}, FE_{NH_3} reaches a maximum of 69.24% at –0.5 V vs. RHE, corresponding to an NH_3 yield rate of 3.76 $mg{\cdot}h^{-1}{\cdot}cm^{-2}$ (Figure 3d). At more negative potentials, the NH_3 selectivity declines, primarily because the accelerated kinetics of the competing HER on the monometallic Ag surface at higher overpotentials and consumes a substantial fraction of electrons. In contrast, the heterometallic Ag_9Cu_6 NC exhibits markedly improved performance across the entire potential window, affording a maximal FE_{NH_3} of 88.48% and an NH_3 yield rate of 9.93 $mg{\cdot}h^{-1}{\cdot}cm^{-2}$ at –0.6 V vs. RHE (Figure 3a). Relative to Ag_{15}, this corresponds to a substantial increase in NH_3 selectivity and an approximately 2.6-fold enhancement in NH_3 yield rate, highlighting the pronounced beneficial effect of site-specific Cu incorporation to generate Ag-Cu microenvironment which facilitates eNO_3RR. The different catalytic behaviors of the two NCs originate from their distinct binding affinities toward key intermediates [14,23]. During electrolysis, Ag_{15} exhibits a non-negligible HER background current accompanied by vigorous H_2 evolution, as reflected in its lower total Faradaic efficiency toward nitrogenous products (FE_{NH_3} + $FE_{NO_2^-}$, Figure 3e). This behavior suggests that proton (*H) adsorption remains relatively facile on the monometallic Ag surface. On the basis of our previous time dependent-density functional theory (TD-DFT) calculations, the lowest unoccupied molecular orbitals in $M_{15}(C{\equiv}C^tBu)_{12})^+$ (M = Au, Ag, Cu) NCs are primarily localized on the Ag_8 cube, whereas the Cu d orbitals contribute significantly to the electronic states below the highest occupied molecular orbital (HOMO) [44,45]. Site-specific Cu doping therefore reconstructs the electronic structure by raising the frontier occupied states and generating a synergic Cu-Ag surface environment. As a result, the heteronuclear surface sites preferentially stabilize nitrogen-containing intermediates such as $*NO_3$ and $*NO_2$ while disfavoring proton capture (Figure 3b). This favorable adsorption, arising from both geometric and energetic effects, effectively suppresses the competing HER and thereby channels electron flux preferentially toward the ammonia formation pathway, highlighting the key role of the Ag–Cu surface microenvironment in steering the reaction selectivity [14,23].

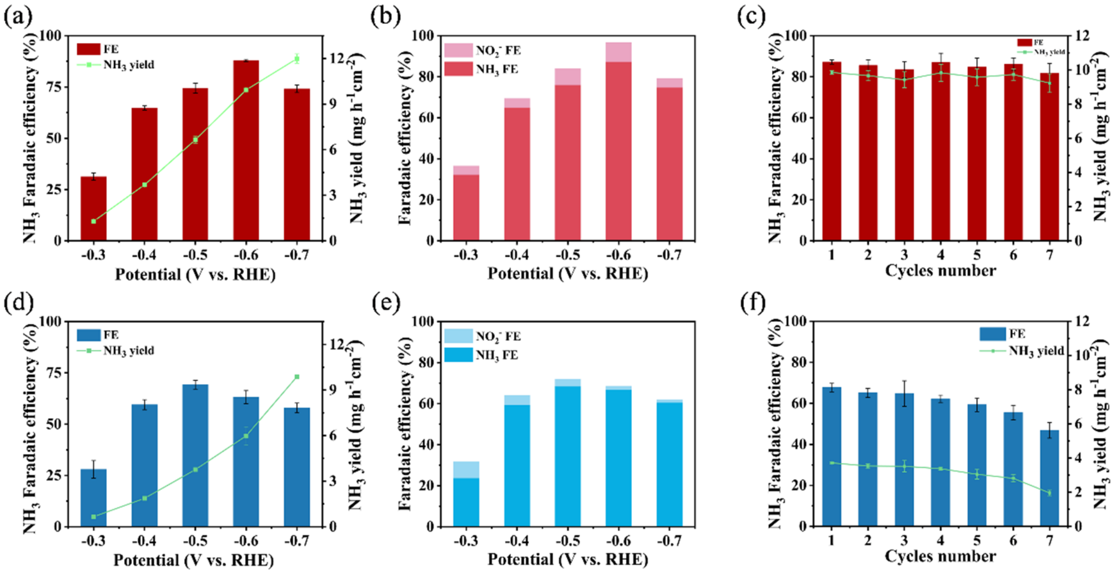

Figure 3. (**a**) FE_{NH_3} and NH_3 yield rate of $Ag_9Cu_6(C{\equiv}C^tBu)_{12}^+$ at various applied potentials. (**b**) NH_3 selectivity of $Ag_9Cu_6(C{\equiv}C^tBu)_{12}^+$ at various applied potentials. (**c**) FE_{NH_3} and the NH_3 yield rate over seven consecutive tests using the Ag_9Cu_6 catalyst at −0.6 V vs. RHE, with the total accumulated charge reaching 800 C in each circle (**d**) FE_{NH_3} and NH_3 yield rate of $Ag_{15}(C{\equiv}C^tBu)_{12}^+$ at various applied potentials. (**e**) NH_3 selectivity of $Ag_{15}(C{\equiv}C^tBu)_{12}^+$ at various applied potentials. (**f**) FE_{NH_3} and the NH_3 yield rate over seven consecutive tests using Ag_{15} catalyst at −0.5 V vs. RHE, with the total accumulated charge reaching 800 C in each circle.

Catalyst stability under operating conditions is equally crucial for practical application. Long-term electrolysis and recycling tests show that, both Ag_9Cu_6 and Ag_{15} retain stable current density over seven consecutive cycles with only minor losses in NH_3 selectivity and yield rate (the total accumulated charge reaching 800 C in each circle, Figure 3c,f). This robustness can be attributed to the structural integrity of the $Ag_1@Ag_8@M_6$ (M = Ag/Cu) framework under strongly reducing conditions, which helps resist catalyst reconstruction and electrochemical dissolution of the active sites.

2.3. Mechanistic Insights

First, we performed a ^{15}N isotope-labeling experiment using 0.1 M $Na^{15}NO_3$ as the reactant, and the products were analyzed by ^1H NMR spectroscopy. As shown in Figure S5 (top), the ^1H NMR spectrum exhibits a clear doublet corresponding to $^{15}NH_4^+$. In contrast, when $K^{14}NO_3$ was used as the reactant, a triplet signal characteristic of $^{14}NH_4^+$ was observed (Figure S5, bottom). These results provide direct and conclusive evidence that the generated ammonia originates from the electroreduction of nitrate, rather than from other nitrogen-containing impurities.

To gain molecular-level insight into the origin of the enhanced eNO_3RR performance of Ag_9Cu_6, *in situ* attenuated total reflection surface-enhanced infrared absorption spectroscopy (ATR-SEIRAS) was employed to monitor the evolution of adsorbed intermediates at the electrode/electrolyte interface (Figure 4). As the applied potential was swept cathodically, characteristic bands assigned to adsorbed nitrate ($*NO_3$), nitrite ($*NO_2$), nitric oxide ($*NO$), hydroxylamine ($*NH_2OH$), ammonia ($*NH_3$), and amino species ($*NH_2$) emerged sequentially for both the catalysts (Figure 4a,b) [18,46–48]. These observations indicate that both Ag_{15} and Ag_9Cu_6 follow the same deoxygenation and hydrogenation sequence in alkaline medium: $NO_3^- \rightarrow *NO_3 \rightarrow *NO_2 \rightarrow *NO \rightarrow *NH_2OH \rightarrow *NH_2 \rightarrow *NH_3 \rightarrow NH_3$.

Although the overall reaction pathway remains identical, the two catalysts differ markedly in the kinetics of their terminal hydrogenation steps. On the Ag_{15} surface, the infrared absorption band corresponding to the $*NH_2$ intermediate (~1625 cm^{-1}) intensifies continuously with increasing cathodic overpotential, whereas the characteristic signal of the final product $*NH_3$ (~1450 cm^{-1}) remains marginal (Figure 4a). This spectroscopic evidence reveals that the final proton-coupled electron transfer (PCET) step ($*NH_2 \rightarrow *NH_3$) is kinetically sluggish on Ag_{15}. Consequently, the severe accumulation of $*NH_2$ blocks the available active sites and impedes overall catalytic turnover, fundamentally accounting for the inferior NH_3 yield of Ag_{15}.

In sharp contrast, the Ag_9Cu_6 catalyst effectively alleviates this kinetic bottleneck (Figure 4b). *In situ* infrared (IR) spectroscopy reveals that the $*NH_2$ signal (~1600 cm^{-1}) does not accumulate significantly at lower potentials. Instead, the $*NH_3$ band (~1450 cm^{-1}) intensifies substantially under increasing cathodic polarization. This spectroscopic evidence indicates that Cu incorporation tailors the local chemical environment to facilitate deep hydrogenation ($*NH_2 \rightarrow *NH_3$). Specifically, the optimized electronic structure originating from the Cu-Ag synergy lowers the activation barrier for the rate-determining $*NH_2$-to-$*NH_3$ conversion—a step that is kinetically hindered on Ag_{15}. Subsequently, the formed $*NH_3$ desorbs readily, regenerating the active sites and sustaining continuous catalytic turnover.

Mechanistically, combining the potentiostatic Faradaic efficiency with the in-situ IR data elucidates the underlying origin of this enhanced performance: the heteronuclear Cu-Ag sites optimize the binding energy of adsorbed hydrogen ($*H$) which serves a dual purpose: (1) it supplies abundant active hydrogen species crucial for the final eNO_3RR hydrogenation step; and (2) it elevates the kinetic barrier for the $*H$ recombination (Tafel step) in the competing hydrogen evolution reaction (HER). Consequently, Ag_9Cu_6 efficiently drives the target eNO_3RR while profoundly suppressing the parasitic HER, effectively overcoming the intrinsic catalytic trade-off between the two pathways.

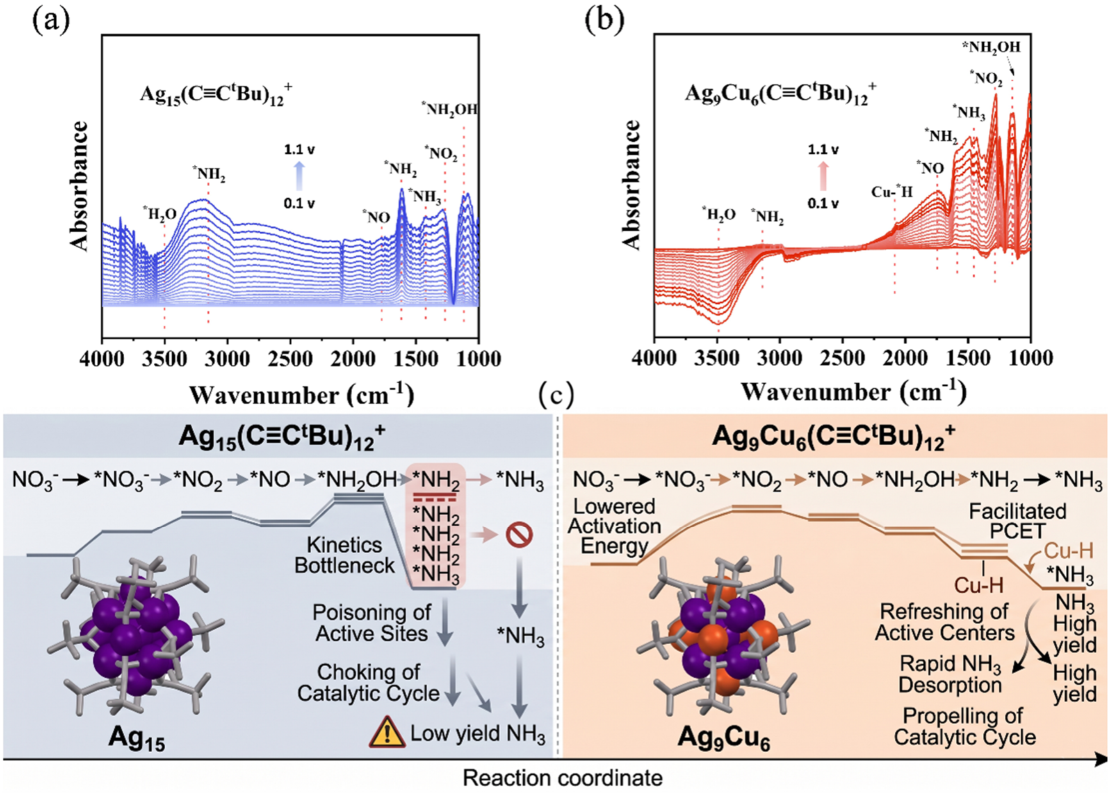

Figure 4. *In situ* IR spectra of (**a**) $Ag_{15}(C{\equiv}C^tBu)_{12}^+$ and (**b**) $Ag_9Cu_6(C{\equiv}C^tBu)_{12}^+$ recorded at various applied potentials during the electrocatalytic process in 1.0 M KOH containing 0.1 M KNO_3. (**c**) Schematic illustration of the proposed eNO_3RR mechanism on Ag_{15} and Ag_9Cu_6.

3. Conclusions

In summary, this work demonstrates that atomically precise nanoclusters provide an effective platform for uncovering the atomic-level role of heterometal doping in eNO_3RR. By comparing monometallic Ag_{15} with bimetallic Ag_9Cu_6 of the same structure, we show that site-specific Cu incorporation at outer positions forms a well-defined rigid $Ag_1@Ag_8@Cu_6$ framework, creating a distinct Cu-Ag surface microenvironment that markedly enhances catalytic performance. As a result, Ag_9Cu_6 achieves an NH_3 Faradaic efficiency of 88.48% and a yield rate of 9.93 $mg \cdot h^{-1} \cdot cm^{-2}$ at –0.6 V vs. RHE, significantly outperforming Ag_{15} while maintaining excellent structural integrity and long-term operational stability. Mechanistic investigations further reveal that Cu doping reconstruct the electronic structure by raising the occupied electronic states, promotes deep hydrogenation of $*NH_2$ to $*NH_3$ (the rate-determining step) and suppresses the competing HER, endowing the nanocatalysts with a distinctive nitrate-philic but proton-phobic character. This study not only identifies a highly efficient Ag-Cu catalyst for selective NH_3 synthesis, but also establishes a clear atomic-level structure-activity relationship that guide the rational design of next-generation bimetallic electrocatalysts.

Supplementary Materials

The additional data and information can be downloaded at: https://media.sciltp.com/articles/others/2606241404462244/eChem-26040166-SM.pdf. Table S1. The comparison between Ag_9Cu_6 and other catalysts in eNO_3RR. Figure S1. (a) The UV-vis absorption spectra for standard $(NH_4)_2SO_4$ solutions with different concentrations in 1 M KOH and (b) corresponding calibration curve for the colorimetric NH_4^+ assay. Figure S2. (a) The UV-vis absorption spectra for standard KNO_2 solutions with different concentrations in 1 M KOH and (b) corresponding calibration curve for the colorimetric NO_2^- assay. Figure S3. Chronoamperometric responses (current density vs. time) of Ag_9Cu_6 under potentiostatic conditions at an applied potential of −0.6 V vs. RHE. All measurements were conducted until the total charge transferred amounted to 800 C. Figure S4. Chronoamperometric responses (current density vs. time) of Ag_{15} under potentiostatic conditions at an applied potential of −0.6 V vs. RHE. All measurements were conducted until the total charge transferred amounted to 800 C. Figure S5. ^1H NMR spectra of eNO_3RR using Ag_9Cu_6 as catalysts and $^{15}NO_3^-$ or $^{14}NO_3^-$ as electrolytes. References [49–56] are cited in supplementary materials.

Author Contributions

J.T.: conducted the experiments; L.Q. (Liang Qiao): performed the characterization; J.T. and Y.L.: wrote the manuscript; J.Y., T.W., L.Q. (Lubing Qin), R.H., and C.Y.: conducted the data analysis; Y.L., K.C. and Z.T.: conceived the project. All authors have read and agreed to the published version of the manuscript.

Funding

This research was funded by the Guangdong Natural Science Funds (No. 2023A0505050107).

Informed Consent Statement

Informed consent was obtained from all individual participants included in the study. Consent to publish was obtained from all individual participants included in this study.

Data Availability Statement

All the necessary data is available in the main text and Supplementary Materials. The data is also available on request from the authors.

Conflicts of Interest

The authors declare no conflicts of interest.

References

1. Ye, D.; Tsang, S.C.E. Prospects and Challenges of Green Ammonia Synthesis. *Nat. Synth.* **2023**, *2*, 612–623.
2. Jiao, F.; Xu, B. Electrochemical Ammonia Synthesis and Ammonia Fuel Cells. *Adv. Mater.* **2019**, *31*, 1805173.
3. Fu, X.; Zhang, J.; Kang, Y. Recent Advances and Challenges of Electrochemical Ammonia Synthesis. *Chem. Catal.* **2022**, *2*, 2590–2613.
4. Long, J.; Chen, S.; Zhang, Y.; et al. Direct Electrochemical Ammonia Synthesis from Nitric Oxide. *Angew. Chem.* **2020**, *132*, 9798–9805.

5. Shen, H.; Choi, C.; Masa, J.; et al. Electrochemical Ammonia Synthesis: Mechanistic Understanding and Catalyst Design. *Chem* **2021**, *7*, 1708–1754.
6. Luo, H.; Li, S.; Wu, Z.; et al. Modulating the Active Hydrogen Adsorption on Fe─N Interface for Boosted Electrocatalytic Nitrate Reduction with Ultra-Long Stability. *Adv. Mater.* **2023**, *35*, 2304695.
7. Zhang, H.; Wang, C.; Luo, H.; et al. Iron Nanoparticles Protected by Chainmail-Structured Graphene for Durable Electrocatalytic Nitrate Reduction to Nitrogen. *Angew. Chem. Int. Ed.* **2023**, *62*, e202217071.
8. Shi, L.; Yin, Y.; Wang, S.; et al. Rational Catalyst Design for N_2 Reduction under Ambient Conditions: Strategies toward Enhanced Conversion Efficiency. *ACS Catal.* **2020**, *10*, 6870–6899.
9. Zhu, X.; Fan, X.; Lin, H.; et al. Highly Efficient Electroenzymatic Cascade Reduction Reaction for the Conversion of Nitrite to Ammonia. *Adv. Energy Mater.* **2023**, *13*, 2300669.
10. Ge, Z.; Wang, T.; Ding, Y.; et al. Interfacial Engineering Enhances the Electroactivity of Frame-Like Concave RhCu Bimetallic Nanocubes for Nitrate Reduction. *Adv. Energy Mater.* **2022**, *12*, 2103916.
11. Qin, L.; Sun, F.; Gong, Z.; et al. Electrochemical NO_3^- Reduction Catalyzed by Atomically Precise $Ag_{30}Pd_4$ Bimetallic Nanocluster: Synergistic Catalysis or Tandem Catalysis? *ACS Nano* **2023**, *17*, 12747–12758.
12. Jia, Y.; Ji, Y.G.; Xue, Q.; et al. Efficient Nitrate-to-Ammonia Electroreduction at Cobalt Phosphide Nanoshuttles. *ACS Appl. Mater. Interfaces* **2021**, *13*, 45521–45527.
13. Xiong, Y.; Wang, Y.; Zhou, J.; et al. Electrochemical Nitrate Reduction: Ammonia Synthesis and Beyond. *Adv. Mater.* **2024**, *36*, e2304021.
14. Wu, Z.; Kang, X.; Wang, S.; et al. Co-Catalytic Metal-Support Interactions Design on Single-Atom Alloy for Boosted Electro-Reduction of Nitrate to Nitrogen. *Adv. Funct. Mater.* **2024**, *34*, 2406917.
15. Dai, Y.; Zheng, X.; Antonietti, M.; et al. Nitrite Reduction at Low Overpotentials on N-Doped Carbon: When Metal Single Atoms Become Poisons. *J. Am. Chem. Soc.* **2025**, *147*, 42874–42882.
16. Wang, Y.; Bao, T.; Chen, L.; et al. Boosting Nitrate-to-Ammonia Conversion over Copper-Based Electrocatalysts by Facilitating Hydrogenation and Product Desorption. *Angew. Chem. Int. Ed.* **2025**, *64*, e202509090.
17. Wu, Q.; Han, Y.; Wu, L.; et al. Constructing Asymmetric Sn-Cu-C Interface via Defective Carbon Trapped Atomic Clusters for Efficient Neutral Nitrate Reduction. *Adv. Mater.* **2025**, *37*, 2505743.
18. Wan, Y.; Tang, Y.; Zuo, Y.; et al. Interfacial Hydrogen-Bond Modulation of Dynamic Catalysts for Nitrate Electroreduction to Ammonia. *Energy Environ. Sci.* **2025**, *18*, 7460–7469.
19. Guo, C.; Shen, L.; Tang, Y.; et al. Ru Single Atoms Anchored on Co-NC for Nitrate Electroreduction toward NH_3 Synthesis. *Nano Res.* **2025**, *18*, 94907623.
20. Guo, C.; Shen, L.Y.; Tang, Y.; et al. Cu Nanowires Encapsulated by ZIF-67 for Efficient Ammonia Electrosynthesis from Nitrate. *ChemSusChem* **2025**, *18*, e202401418.
21. Qin, L.; Sun, F.; Li, M.; et al. Atomically Precise $(AgPd)_{27}$ Nanoclusters for Nitrate Electroreduction to NH_3: Modulating the Metal Core by a Ligand Induced Strategy. *Acta Phys. Chim. Sin.* **2025**, *41*, 100008.
22. He, Q.; Shi, Z.; Yu, D.; et al. Dynamic Reconstruction and Microenvironment Modulation of a Pd-Doped CuS Electrocatalyst for Nearly Unity-Efficiency Ammonia Electrosynthesis from Nitrate. *J. Am. Chem. Soc.* **2025**, *147*, 43067–43076.
23. Zhu, X.; Wang, Y.C.; Qu, K.; et al. Modulating Ru-Co Bond Lengths in Ru_1Co Single-Atom Alloys through Crystal Phase Engineering for Electrocatalytic Nitrate-to-Ammonia Conversion. *Nat. Commun.* **2025**, *16*, 5742.
24. Wei, J.; Li, C.; Sun, Z.; et al. Nitrogen-Rich MOF-Material-Derived Metal Dual-Atom Platforms for Efficient Electrochemical Nitrate Reduction. *Angew. Chem. Int. Ed.* **2025**, *137*, e202517259.
25. Zhu, Y.; Li, Y.; Tian, Y.; et al. DFT-Guided Design and Synthesis of Bipyridine-Anchored Copper Single-Atom Catalysts for Efficient Nitrate-to-Ammonia Electroreduction across a Broad pH Range. *Angew. Chem. Int. Ed.* **2026**, *138*, e202517715.
26. Ge, Y.; Sun, L.; Xu, X.; et al. Charge-Spin-Orbit Modulated Carbon-Encapsulated FeP/Fe_3O_4 Heterojunctions for Ultrafast and Stable Conversion of Low-Concentration Nitrate to Ammonia. *Angew. Chem. Int. Ed.* **2026**, *138*, e202519571.
27. Wang, Y.; Wang, S.; Fu, Y.; et al. Ammonia Electrosynthesis from Nitrate Using a Stable Amorphous/Crystalline Dual-Phase Cu Catalyst. *Nat. Commun.* **2025**, *16*, 897.
28. Liu, M.; Qi, J.; Luo, G.; et al. Asymmetric N,S-Coordinated Cu Single-Atom Catalysts for High-Performance Electrocatalytic Nitrate-to-Ammonia. *Adv. Funct. Mater.* **2025**, *35*, e23666.
29. Dong, H.; Ye, J.; Liu, X.; et al. Spatially Separated Ag@Cu_3N Tandem Electrocatalyst with High Nitrate-to-Ammonia Selectivity via Decoupled Deoxygenation-Hydrogenation Pathway. *Adv. Funct. Mater.* **2025**, *35*, e26882.
30. Zhang, L.; Liu, Y.; Li, L.; et al. Aryl Sulfur Ligand-Modulated Silver Catalysts with Tailored Binding Affinity for Selective Nitrate-to-Ammonia Conversion. *Nat. Commun.* **2026**, *17*, 2553.
31. Wu, Z.; Shi, Z.; Xie, F.; et al. Tandem Catalysis Enables High-Rate Nitrate Electroreduction via Interfacial Water Regulation. *Adv. Mater.* **2026**, *38*, e25072651.
32. Li, D.; Chai, Y.; Xiao, Q.; et al. Confinement-Induced Enrichment in Hollow Multishelled Structure for High-Efficiency Ammonia Electrosynthesis. *J. Am. Chem. Soc.* **2026**, *148*, 17910–17919.

33. Li, Q.; Li, Y.; Xu, B.; et al. Gram-Scale Ammonia Synthesis via Electrochemical Nitrate Reduction Using Enzyme-Inspired Dual-Atomic Cu Catalyst. *Angew. Chem. Int. Ed.* **2025**, *64*, e202510139.
34. Liu, X.; Xiang, T.; Liu, J.; et al. Ag Single Atoms Boosting Water Dissociation on Cu Nanowires for Efficient H-Mediated Nitrate Reduction at Ultra-Low Concentrations with Ammonia Recovery. *Adv. Funct. Mater.* **2026**, *36*, e241402.
35. Chen, M.; Guo, C.; Qin, L.; et al. Atomically Precise Cu Nanoclusters: Recent Advances, Challenges, and Perspectives in Synthesis and Catalytic Applications. *Nano-Micro Lett.* **2024**, *17*, 83.
36. Chen, M.Y.; Shen, L.Y.; Qin, L.B.; et al. Atomically Precise Cu_6 Nanoclusters for Oxygen Evolution Catalysis: A Combined Experimental and Theoretical Study. *Rare Met.* **2025**, *44*, 2428–2437. (In Chinese)
37. Liu, Z.; Li, S.; Zhao, L.; et al. Alkynyl-Protected Cu_{67} Nanocluster Superatom: Structure Anatomy and Electrochemical CO_2 Reduction Study. *Nano Res.* **2026**, *19*, 94908145.
38. Liu, Z.; Zhu, P.; Zhou, X.; et al. Atomically Precise Cu_{14} and Cu_{13} Nanoclusters for the Oxygen Evolution Reaction: One Additional Cu Atom Matters. *Inorg. Chem. Front.* **2025**, *12*, 4606–4612.
39. Zuo, D.; Pan, C.; Chen, Z.; et al. One Atom Makes a Big Difference in NHC-Ligated Alloy Nanoclusters: From Structure and Properties to Catalysis. *Angew. Chem. Int. Ed.* **2026**, *65*, e202500123.
40. Lin, C.L.; Lei, X.; Zhang, Y.; et al. Controlling Chirality and Stability of Gold Nanoclusters by PNP Pincer Ligand Diastereomers. *Nano Lett.* **2025**, *25*, 11374–11381.
41. Sun, F.; Zhou, X.; Qin, L.; et al. Probing Temperature Effect on Enhanced Electrochemical CO_2 Reduction of Hydrophobic $Au_{25}(SR)_{18}$ Nanoclusters. *ACS Catal.* **2025**, *15*, 4605–4617.
42. Lai, X.X.; Wei, J.; Liu, T.T.; et al. Atomically Precise Gold Nanocluster Boosting Selective Hydrogenation of Nitroarene by H_2 in Water. *Nat. Commun.* **2025**, *16*, 7862.
43. Wang, L.; Chen, L.; Qin, L.; et al. Alkynyl-Protected $Ag_{20}Rh_2$ Nanocluster with Atomic Precision: Structure Analysis and Tri-Functionality Catalytic Application. *Chem. Asian J.* **2023**, *18*, e202300685.
44. Qin, L.; Sun, F.; Ma, X.; et al. Homoleptic Alkynyl-Protected Ag_{15} Nanocluster with Atomic Precision: Structural Analysis and Electrocatalytic Performance toward CO_2 Reduction. *Angew. Chem. Int. Ed.* **2021**, *60*, 26136–26141.
45. Ma, X.; Xiong, L.; Qin, L.; et al. A Homoleptic Alkynyl-Protected $[Ag_9Cu_6(^tBuC{\equiv}C)_{12}]^+$ Superatom with Free Electrons: Synthesis, Structure Analysis, and Different Properties Compared with the Au_7Ag_8 Cluster in the M_{15}^+ Series. *Chem. Sci.* **2021**, *12*, 12819–12826.
46. Ouyang, X.; Qiao, W.; Yang, Y.; et al. Intensifying Interfacial Reverse Hydrogen Spillover for Boosted Electrocatalytic Nitrate Reduction to Ammonia. *Angew. Chem. Int. Ed.* **2025**, *64*, e202422585.
47. Qin, L.; Chen, Y.; Liu, Z.; et al. Construction of Atomic-Scale Compressive Strain for Oxime Electrosynthesis. *J. Am. Chem. Soc.* **2025**, *147*, 18003–18016.
48. Zuo, Y.; Sun, M.; Li, T.; et al. Capturing Copper Single Atom in Proton Donor Stimulated O-End Nitrate Reduction. *Adv. Mater.* **2025**, *37*, 2415632.
49. Ma, G.; Sun, F.; Qiao, L.; et al. Atomically Precise Alkynyl-Protected $Ag_{20}Cu_{12}$ Nanocluster: Structure Analysis and Electrocatalytic Performance toward Nitrate Reduction for NH_3 Synthesis. *Nano Res.* **2023**, *16*, 10867–10872.
50. Wang, J.; Cai, J.; Ren, K.-X.; et al. Stepwise Structural Evolution toward Robust Carboranealkynyl-Protected Copper Nanocluster Catalysts for Nitrate Electroreduction. *Sci. Adv.* **2024**, *10*, eadn7556.
51. Liu, X.; Liu, J.; Chen, A.; et al. 99.7% Faradaic Efficiency in Nitrate Reduction Enabled by Defect-Rich Copper Nanoparticles. *ACS Appl. Nano Mater.* **2025**, *8*, 17518–17526.
52. Zhang, B.; Dai, Z.; Chen, Y.; et al. Defect-Induced Triple Synergistic Modulation in Copper for Superior Electrochemical Ammonia Production across Broad Nitrate Concentrations. *Nat. Commun.* **2024**, *15*, 2816.
53. Feng, Z.; He, Y.; Cui, Y.; et al. Efficient Tandem Electrocatalytic Nitrate Reduction to Ammonia on Bimodal Nanoporous Ag/Ag–Co across Broad Nitrate Concentrations. *Nano Lett.* **2024**, *24*, 11929–11936.
54. Jia, R.; Zhang, X.; Gan, L.; et al. Boosting Electrocatalytic Nitrate Reduction to Ammonia with a Cu/Ag-Ru Tandem Catalyst at Industrial-Scale Current Density. *J. Mater. Chem. A* **2025**, *13*, 5732–5743.
55. Meng, Z.; Wang, S.; Li, Y.; et al. Tandem Catalysis Facilitates Nitrate-to-Ammonia Electroreduction on AgCu Telluride Nanowires. *Sci. China Chem.* **2026**, *69*, 2331–2337.
56. Kui, B.; Zhao, S.; Hu, Y.; et al. Strongly Coupled Ag/Cu with MXene for Efficient Tandem Nitrate Reduction Reaction and Zinc–Nitrate Batteries. *Catal. Sci. Technol.* **2025**, *15*, 1617–1626.